

# Light Modelling and Calibration in Laparoscopy

**Richard Modrzejewski · Toby Collins ·  
Alexandre Hostettler · Jacques  
Marescaux · Adrien Bartoli**

Received: date / Accepted: date

## Abstract

**Purpose.** A better understanding of photometry in laparoscopic images can increase the reliability of computer-assisted surgery applications. Photometry requires modelling illumination, tissue reflectance and camera response. There exists a large variety of light models, but no systematic and reproducible evaluation. We present a review of light models in laparoscopic surgery, a unified calibration approach, an evaluation methodology, and a practical use of photometry.

**Method.** We use images of a calibration checkerboard to calibrate the light models. We then use these models in a proposed dense stereo algorithm exploiting the shading and simultaneously extracting the tissue albedo, which we call dense shading stereo. The approach works with a broad range of light models, giving us a way to test their respective merits.

**Results.** We show that overly complex light models are usually not needed and that the light source position must be calibrated. We also show that dense shading stereo outperforms existing methods, in terms of both geometric and photometric errors, and achieves sub-millimeter accuracy.

**Conclusion.** This work demonstrates the importance of careful light modelling and calibration for computer-assisted surgical applications. It gives guidelines on choosing the best performing light model.

**Keywords** Light Modelling · Surface Reconstruction · Densification Method · Multi View Stereo

---

Richard Modrzejewski  
EnCoV, Institut Pascal, UMR 6602, CNRS/UBP/SIGMA, 63000 Clermont-Ferrand  
E-mail: Richard.modrzejewski@uca.fr

Toby Collins  
IRCAD and IHU-Strasbourg, 1 Place de l'Hopital, 67000 Strasbourg  
E-mail: Toby.collins@ircad.fr

## 1 Introduction: Clinical Motivation and Existing Works

Augmented reality (AR) in laparoscopic surgery is a major task, widely studied over the last decade [6, 3, 5, 10]. Nevertheless, while AR is solved in some non-medical applications, laparoscopic surgery lags behind because of complicating factors such as lack of texture, strong deformations and illumination changes. The general AR pipeline for laparoscopy has five main stages [6]: 1) preoperative organ model reconstruction from volumetric data, 2) intraoperative 3D organ reconstruction, 3) reconstruction scale estimation 4) deformable registration and model texturing, and 5) deformation tracking. Photometric cues may be used to overcome the previously described difficulties, at all stages except 1). For the sake of clarity, we here focus on stage 2). The intra-operative 3D organ reconstruction is computed from an exploration video captured at the beginning of surgery. However, the quality of the reconstruction obtained with Structure-from-Motion (SfM) or Simultaneous Localization and Mapping (SLAM) [14] is often poor, thus limiting the accuracy of AR. Because using photometry, and in particular shading, considerably improves dense 3D reconstruction in outdoor scenes [12], it is important to attempt a similar approach to move ahead in laparoscopy.

The main current challenge to use photometry in laparoscopy is light modelling. In laparoscopy, the primary light source is fixed relative to the camera, making the problem of light modelling far more constrained than in the general case. Therefore, the use of a calibrated light model is particularly appropriate. Prior work using photometry in laparoscopy is about Shape-from-Shading (SfS) [18, 7, 5], photometric stereo [4, 19] and dense stereo [20]. The complexity of the light models greatly varies, from simple ones [19, 3, 10] to much more advanced ones [4, 5]. However, choosing the best light model is never discussed explicitly. How does this choice affect the result of the application? What are the differences in terms of accuracy for the different illumination models? To which extent should they be calibrated? Can a unified calibration approach be applied? Answers to these questions are missing and they are fundamental to make progress with photometry in laparoscopy.

To answer these questions, we present models for laparoscopic light and ways to calibrate them. We discuss and compare these models in terms of complexity and accuracy. We then present a practical usage of photometric laparoscopy in dense stereo and albedo estimation.

## 2 Modelling Photometry in Laparoscopy

### 2.1 General Shading Equation

Each colour channel constraints the problem, but in order to avoid clutter in the notation, we consider only one channel as image  $I$ . We express the link between the pixel intensity image  $I(p)$  and the properties of the observed

object. The general shading equation is:

$$I(p) = \mathcal{C} \circ F(\rho(x), \sigma(x), \mathbf{n}(x)), \quad (1)$$

where the image point  $p$  corresponds to a 3D point  $x$  of the surface,  $\sigma(x)$  is the light vector that corresponds to the light received by the surface at  $x$ ,  $\rho(x)$  and  $\mathbf{n}(x)$  are the albedo and the normal at  $x$ ,  $F$  is the reflectance model of the material giving irradiance, and  $\mathcal{C}$  is the camera response function (CRF).

## 2.2 Camera Response Models

For one image, the CRF is usually a simple gain  $\mathcal{C}'(p)$  depending only on the position of the image point [19, 5, 8]:

$$I(p) = \mathcal{C}'(p) F(\rho(x), \sigma(x), \mathbf{n}(x)). \quad (2)$$

The gain  $\mathcal{C}'(p)$  is generally split in two terms [2]: one linear and one radial term. The linear term depends on the aperture of the camera and on the normalisation of the raw intensity. The radial term, mainly modeling vignetting, is caused by the lens. It corresponds to the attenuation of brightness away from the image center. We only consider the linear term, as the radial term is, when camera and light axes are similar, redundant with the term denoting the principal direction of light propagation. In many works [12, 13],  $\mathcal{C}'$  is assumed not to differ between views. For most laparoscopes however,  $\mathcal{C}'$  varies greatly between images, because of auto-exposure. This is important as it gives the surgeon the best image quality at any moment. It is thus a difficulty for using photometry:  $\mathcal{C}'$  has to be determined on the fly for each view independently. If  $k$  is the image index, we have  $\mathcal{C}'_k(p) = \mathcal{C}_k$  and equation (2) becomes:

$$I_k(p) = \mathcal{C}_k F(\rho(x), \sigma(x), \mathbf{n}(x)). \quad (3)$$

## 2.3 Surface Reflectance

Reflectance describes how a surface material reflects incident light. Many models consider that this term has two components, namely the diffuse and specular components. Specular reflection is the light reemitted preferentially around one principal direction. This creates localised saturated areas in the image called specularities. The diffuse component corresponds to the light which is reflected equally in all directions. In laparoscopy, while some works consider advanced reflectance models such as Cook-Torrance [16], the diffuse lambertian reflectance is usually enough [10, 3]. Indeed, with wet tissues the specularities form tight isolated spots, removable by a simple saturation test [4]. For lambertian reflectance, we have  $F(\rho(x), \sigma(x), \mathbf{n}(x)) = \rho(x) \sigma(x) \cdot \mathbf{n}(x)$  and equation (3) becomes:

$$I_k(p) = \mathcal{C}_k \rho(x) \sigma(x) \cdot \mathbf{n}(x). \quad (4)$$

## 2.4 Light Models

**Point models.** The laparoscope light is often modelled as a point  $P$  [10, 3] that we call the *light centre*. Without preferential direction of light propagation, this is the Point Light Source model (PLS). At point  $x$ , the normalised light direction is:

$$\mathbf{L}(x, P) = \frac{x - P}{\|x - P\|}. \quad (5)$$

Using the inverse square law spherical fall-off model  $\mathbf{S}(x, P) = \frac{1}{\|x - P\|^2}$ , and defining  $\sigma_0$  as the main intensity value, we arrive at the PLS model as:

$$\sigma_{\text{PLS}}(x, P) = \sigma_0 \mathbf{S}(x, P) \mathbf{L}(x, P). \quad (6)$$

This model has only 3 parameters (the light centre coordinates). In most laparoscopes, light is transmitted to the tip using fibre optics, creating a principal light direction. This, however, is not supported by the PLS model. The Spot Light model (SLS) extends PLS using two extra notions: the principal direction  $D$ , and the light spread factor  $\mu$  which leads to a model with 6 parameters. They are used to create a radial attenuation term  $\mathbf{R}(\mu, D, x, P) = \exp(-\mu(1 - D \cdot \mathbf{L}(x, P)))$ . The SLS model is then:

$$\sigma_{\text{SLS}}(x, P) = \sigma_0 \mathbf{R}(\mu, D, x, P) \mathbf{S}(x, P) \mathbf{L}(x, P). \quad (7)$$

In an attempt to produce more accurate light modelling, SLS has been recently generalised to the Polynomial Spot Light Source (PSLS) of degree  $(p, q)$ :

$$\sigma_{\text{PSLS}}(x, P) = \sum_{i=0}^p \sum_{j=0}^q b_{i,j} (\mathbf{R}(\mu, D, x, P))^i (\mathbf{S}(x, P))^j \mathbf{L}(x, P). \quad (8)$$

In our comparison tests we use  $p = q = 4$ , following [4]. The model has  $(p+1)(q+1) + 6$  parameters, corresponding to the polynomial coefficients  $b_{i,j}$ , the light centre  $P$ , the principal direction  $D$  and the spread factor  $\mu$ .

**The Area Light Source model.** For most laparoscopes, the light source is not a small point, but rather a region extending over the laparoscope's tip that we call light motif, as shown in Fig 1. An obvious extension of point models is thus to consider a set of point lights  $\sigma_p$  distributed over the laparoscope's tip  $\psi$ . This defines the general extended light model:

$$\sigma_{\text{extended}}(x) = \int_{P \in \psi} \sigma_p(x, P) dP. \quad (9)$$

Discretising  $\psi$  to a finite point set  $\psi'$  and considering SLS models sharing their intensity, spread, and direction of propagation leads to the Area Light Source model (ALS):

$$\sigma_{\text{ALS}}(x) = \sigma_0 \sum_{P \in \psi'} \mathbf{R}(\mu, D, x, P) \mathbf{S}(x, P) \mathbf{L}(x, P). \quad (10)$$

### 3 Light Calibration

#### 3.1 Context and Preliminary Remarks

The previously described models need to be calibrated. The main parameter to estimate for point models is the light centre  $P$ . A natural assumption is that  $P$  coincide with the optical centre [3, 10]. This however leads to important illumination modelling errors [4] as also shown in our experiments. The estimated light centre does generally not lie at the physical point of light emission on the laparoscope. In a similar way, when we calibrate a camera, the centre of projection does not generally lie at the physical centre of the camera lens. Indeed, due to the light's aperture (similarly to camera aperture) the light centre exists behind the point of light emission. We calibrate the light centre jointly with the other parameters, including the principal direction of propagation and the spread, in a unified calibration setup described in section 3.2. For the ALS model the light motif is extracted in a preliminary step described in section 3.3.

#### 3.2 General Calibration Method

We consider  $n$  images  $I_k$ ,  $k = 1, \dots, n$ , of a standard diffuse calibration checkerboard. The albedo  $\rho_w$  inside the white squares is unknown but assumed constant. Using the existing camera calibration library from OpenCV, we automatically determine the 3D position of each point  $x$  on the checkerboard and its corresponding normal vector  $\mathbf{n}(x)$ . We then find the photometric parameters that best explain, in the generative least-squares sense, the intensity  $I_k(x)$  of each pixel within the white squares areas, discretised to the pointsets  $W_k$ . We formulate the problem as energy minimisation  $\min_{V, \mathcal{C}} E_{\text{calib}}(V, \mathcal{C})$ , where  $\sigma$  is the light model to calibrate,  $V$  its parameters and  $\mathcal{C} = \{\mathcal{C}_1, \dots, \mathcal{C}_n\}$  the camera response gains:

$$E_{\text{calib}}(V, \mathcal{C}) = \sum_{k=1}^n \sum_{x \in W_k} \left( I_k(x) - \frac{\rho_w \sigma(x, V) \cdot \mathbf{n}(x)}{\mathcal{C}_k} \right)^2. \quad (11)$$

When considering this problem with  $\rho_w$  and all the  $c_k$  unknown, it leads to a scalar ambiguity on all these terms. In order to resolve this ambiguity, we chose a reference image and fix its camera response to 1. We then minimise  $E_{\text{calib}}$  using the Levenberg-Marquardt algorithm as implemented in Ceres [1]. For point models, the light centre  $P$  is initialised at the optic centre,  $D$  as the perpendicular to the image plane and the spread to a large value of  $\mu = 10$ . By inverting the shading equation for this image, we obtain an initial estimate of  $\rho_w$  and for the other images, we estimate the  $\mathcal{C}_k$ .

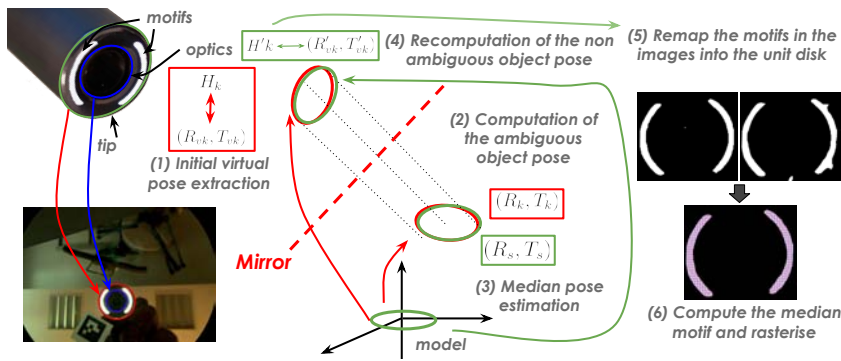
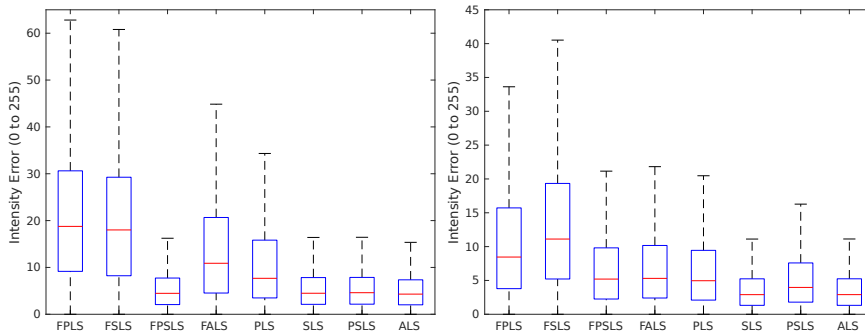


Fig. 1 Extraction of the light area using mirror: from the mirror images to the final motif.

### 3.3 Motif Extraction for the Area Light Source Model

**Principle of the method.** The ALS model requires one to extract the light motif. Our procedure (Fig. 1) is designed for a laparoscope with flat tip and planar light area. Using a mirror, we take  $n$  self-images of the tip of the laparoscope from different orientations. ArUco markers [9] are taped on the mirror in order to compute its pose relative to the camera. We manually annotate the borders of the tip and of the camera optics, to which we fit ellipses. We then use these ellipses to compute the pose of the tip of the laparoscope. For that, we consider the poses of a virtual disc that corresponds to the symmetric of the tip through the mirror. These poses are computed by decomposing the homographies [15] that transform the unit circle into the corresponding ellipses.

**Pose computation.** As we use images of a disc, two ambiguities hold on the pose: one rotation around the main axis and one two-way perspective ambiguity. Both can be solved by exploiting the particularities of our mirror setup. We follow 6 steps. (1) Using the tip ellipse and knowing the tip size, we extract two homographies [17] that transform the unit circle into this ellipse and that correspond to the two possible poses. Using the optics ellipse, we solve the perspective ambiguity and keep only one homography  $H_k$  per image, associated with the virtual pose  $(R_{vk}, T_{vk})$  [15], but the rotation ambiguity remains. (2) Next, using the markers, we compute, by symmetry, the pose of tip  $(R_k, T_k)$ . (3) We then compute the median position of the centre of the tip and its up vector, and we choose one suitable orientation  $(R_s, T_s)$  for those values. (4) We then recompute, by symmetry, the poses of the virtual disks  $(R'_{vk}, T'_{vk})$ , removing the rotation ambiguity we had before. Those poses correspond to homographies  $H'_k$ . (5) Finally, the light region is extracted from each image as the saturated pixels and mapped into the same reference view using the homographies. By taking the median of all these remapped light areas, we obtain the final 2D light motif. (6) We then discretise it, and use the position of the support object disc to obtain a set of  $m$  3D points corresponding to our



**Fig. 2** Boxplot showing the difference between the observed and predicted pixel intensities: Short Range images (left) and Medium Range images (right).

$m$  point light sources, defined in 3D camera coordinates. We use  $m = 237$  in our experiments.

### 3.4 Light Model Comparison

We used two main sets of images for the evaluation. The first is a ‘medium-range set’ containing images of a medium sized checkerboard ( $30 \times 15$  mm) seen at a medium distance ( $\approx 50$  mm). In this configuration, we expect the modelling of our source as a point to be valid. The second is the ‘close range set’ with a small checkerboard ( $12 \times 6$  mm) seen at a short distance ( $\approx 10$ - $15$  mm) and where the point models should be faulty. For each set, we split the data in two disjoint sets for calibration and evaluation. We use PLS, SLS, PSLS and ALS to denote the light models with all their parameters calibrated. We use FPLS, FSLs, FPSLS and FALS to denote the models using a fixed light centre at the optical center for point models and a fixed pose as extracted in section 2.3 for the ALS model. The calibrated light centre for PLS and SLS tends to be slightly behind the camera centre, approximately on the camera axis, away from the laparoscope tip. For PSLS, the results are more fluctuating with positions not always found on the camera axis.

For comparing the light models, we consider the absolute difference between the observed and predicted intensities by the calibrated models, for the white squares pixels, as presented in Fig. 2. We observe that calibrating the light centre leads to a general improvement of all models, except PSLS which is on par with FPSLS. Overall, no models perform much better than SLS. Furthermore, when considering a calibrated centre, we observe that the most complex models ALS and PSLS do not perform significantly better than SLS, which is thus a good compromise between complexity and accuracy, even in the close range configuration. We also notice that PSLS does not always give results as good as SLS, which tends to indicate that it does not generalise as well.

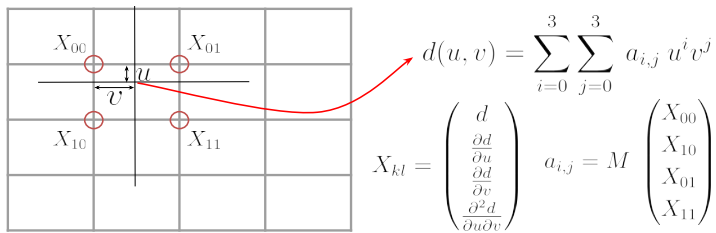


**Fig. 3** Representation of the reconstructed surface by interpolating a depth grid.

## 4 Application to Joint Surface Densification and Albedo Extraction

### 4.1 Overview

In order to show a practical usage of photometry and to compare the light models, we have developed a dense shading stereo algorithm inspired by [12]. This aims at refining a surface reconstruction and unlike other methods [19, 4], does not require any hardware modifications. In [12], general indoor scenes are considered. Consequently, lighting is unknown and has to be estimated along with the reconstruction. In contrast, in our method, a light model is chosen from section 2, and calibrated before considering the reconstruction. This leads to a reduction of the unknowns and an increase of the robustness.

### 4.2 Inputs and Surface Representation

The inputs of our algorithm are a sparse point-cloud  $P_{sp}$  and its keyframes (camera poses and images). These are computed from SfM (we use the proprietary SfM software Photoscan<sup>1</sup> v1.1.6.2038 in high accuracy mode, with pair selection deactivated, keypoint limit set to 40000 and tie point limit set to 1000). We then consider one reference view, and our task is to compute *i*) a dense 3D reconstruction with respect to this view, and *ii*) the albedo of each pixel in the view. We model pixel albedo with an unknown value per pixel and we model depth using bi-cubic patches over a depth grid (Fig. 3). The grid is defined by its nodes, containing the depth value, its first-order derivative in the two spatial dimensions and its mixed derivative. Each patch is a degree 9 polynomial in  $(u, v)$  whose coefficients depend on 4 nodes defining the patch. The interpolated surface is  $C^1$  and its normal at  $(u, v)$  is expressed as a function of the four surrounding nodes. We denote as  $\mathcal{G}$  a set of points uniformly distributed on this surface. The grid size matches the image resolution.

<sup>1</sup> <https://www.agisoft.com>

### 4.3 Dense Shading Stereo

We pose the problem as an energy minimisation acting on the grid nodes  $\mathcal{N}$ , the albedo values  $\rho$  and the camera responses  $\mathcal{C}$  with three terms:

$$E_{\text{rec}}(\rho, \mathcal{D}) = E_{\text{shad}}(\rho, \mathcal{D}) + \lambda_{\text{pos}} E_{\text{pos}}(\mathcal{D}) + \lambda_{\text{reg}} E_{\text{reg}}(\mathcal{D}). \quad (12)$$

The two weights are fixed to  $\lambda_{\text{pos}} = 50$  and  $\lambda_{\text{reg}} = 40$  and the three terms are discussed below. The shading energy  $E_{\text{shad}}(\rho, \mathcal{D})$  denotes the difference, for each point in  $\mathcal{G}$ , between the pixel intensities in the keyframes  $I_k$  and in the images predicted from the reconstruction. This energy uses a weight inspired by [12]: for strong gradient image areas, we use a lower weight because of the lack of reliability of shading in these conditions. Indeed, following the intuition behind the retinex theory [11], shading generates only small intensity changes on smooth surfaces. Additionally, keypoints tend to occur at strong image gradients, leading to reconstructed points in the input reconstruction and thus, naturally creating position constraints in these areas. If  $p_k$  is the projection of  $x$  in the  $k$ -th keyframe,  $A_k$  the object mask in keyframe  $I_k$  and  $\nabla I_r$  the gradient of the reference image  $I_r$ , we have:

$$E_{\text{shad}}(\rho, \mathcal{D}) = \sum_{x \in \mathcal{G}} \exp\left(-\|\nabla I_r(p_r)\|^2\right) \sum_{k=0}^n A_k(p_k) \left(\frac{\rho(x) \sigma(x) \cdot \mathbf{n}(x)}{\mathcal{C}_k} - I_k(p_k)\right)^2. \quad (13)$$

The position energy  $E_{\text{pos}}(\mathcal{D})$  corresponds to sparse depth constraints between the depth grid and  $P_{\text{sp}}$ . If  $d(u, v)$  is the value of the depth at  $(u, v)$ , we have:

$$E_{\text{pos}}(\mathcal{D}) = \sum_{p \in P_{\text{sp}}} ((p_r)_z - d(p_r))^2. \quad (14)$$

The regularization term  $E_{\text{reg}}(\mathcal{D})$  prevents noise in the reconstruction. It considers, for points in  $\mathcal{G}$ , the norm of the second order depth derivatives:

$$E_{\text{reg}}(\mathcal{D}) = \sum_{X \in \mathcal{G}} \left( \left(\frac{\partial^2 d}{\partial^2 u}(X)\right)^2 + \left(\frac{\partial^2 d}{\partial^2 v}(X)\right)^2 + \left(\frac{\partial^2 d}{\partial u \partial v}(X)\right)^2 \right). \quad (15)$$

We initialise the unknowns as follows. The depth grid  $\mathcal{G}$  is initialised by projecting the sparse input point cloud in the reference view. This grid is then smoothed by an intermediate minimisation problem where only  $E_{\text{pos}}$  and  $E_{\text{reg}}$  are considered. Next, we project this initial depth in each keyframe and invert the shading equation for each pixel, to compute albedo candidates. The albedo map is then initialised with the median values of the corresponding candidates. We then perform the minimisation of  $E_{\text{rec}}$ . For both minimisations, we used the Levenberg-Marquardt algorithm implemented using Ceres.

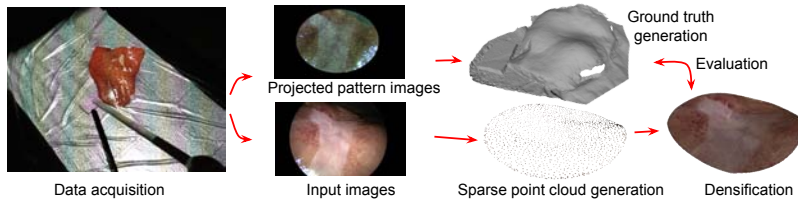


Fig. 4 Building the evaluation ex-vivo dataset using a projected light pattern.

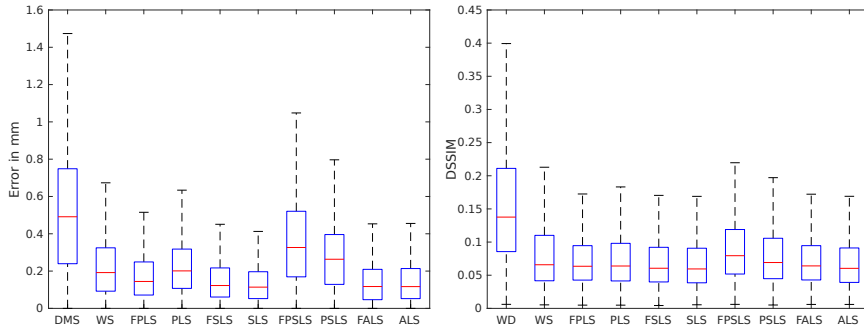


Fig. 5 Photometric error obtained with SLS: target (left), image generation inside the green circle (middle), DSSIM (right).

#### 4.4 Evaluation

**Evaluation data.** We tested our algorithm with ex-vivo bovine liver data. The experimental setup is shown in Fig. 4. A projector casting a dense random pattern was installed over the scene. The laparoscope was attached to a mechanical arm and moved in different configurations. For each of those, we took two images, one with the pattern but without the laparoscope light and one without the pattern but with the light. The first set of images (with the pattern) was used to generate a high quality ground-truth surface using Photoscan (using with the previously described parameters for the SfM step, followed by densification in high accuracy mode with an aggressive depth filtering strategy and meshing using arbitrary surface reconstruction type, high number of faces and interpolation enabled). The second set of images (without the pattern) was split in small subsets of approximately 10 images. These subsets were used to generate sparse input reconstructions to initialise our algorithm, also using Photoscan (still using the same parameters for the SfM but without the densification step). Because of the small number of images and of not using densification, these reconstructions were sparse and noisy. We then compared the reconstructions obtained using our algorithm with different light models, but also using two other configurations. As an ablation study, the first one considers directly the results obtained from Photoscan with densification activated (DMS). The second one considers a reconstruction obtained using our algorithm with only the position and regularisation energies (WS). For both of these methods, the colour of the points were computed a posteriori by taking the median of the image projected points from the reconstruction.

**Evaluation metrics.** We used two metrics to evaluate the results. The first one is the geometric error, defined as the absolute difference in mm between



**Fig. 6** Boxplot showing the reconstruction errors using a large amount of calibration images: geometric (left) and DSSIM (right).

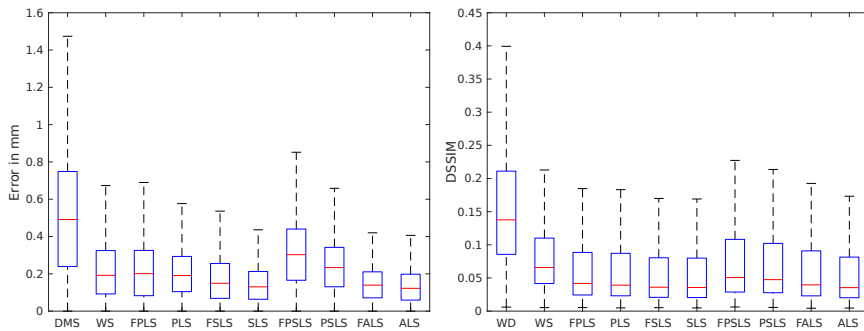


**Fig. 7** Boxplot showing reconstruction errors using a small amount of calibration images: geometric (left) and DSSIM (right).

each pixel’s estimated depth and its ground-truth depth. The second one is the photometric error, corresponding to the average dissimilarity between the keyframes and the images generated using the shading equation (4). Here, the pixel-to-pixel error is not relevant as even a small camera misalignment strongly increases the error. Therefore, we used structural dissimilarity (DSSIM) instead [21]. This is illustrated in Fig. 5. For DMS and WS, as no camera responses were available directly, they had to be extracted first in order to be able to generate images and to consider the photometric error. For that purpose, the depth grid was projected to the images and for each point, we computed the ratio between the colour in the reconstruction and in the image. We then set the camera response as the median of the ratios over the visible points.

**Results.** We considered grids with  $65 \times 65$  nodes associated with  $1920 \times 1080$  depthmaps. We divided the evaluation into two sets of images to calibrate the light: a small one (approximately 15 images, leading to less precise calibration) and a large one (approximately 60 images, leading to more precise calibration). This was done in order to observe the influence of better calibration for each

light model. The results are presented in Fig. 6 and 7. The surfaces considered for the reconstructions are circular patches with a diameter of approximately 50 mm and are seen at a distance of between 20 and 40 mm. Our tests were run on an Intel<sup>®</sup> Xeon<sup>®</sup> E5-1620 with non-optimized C++ code with 6 threads allocated for the non-linear optimisation. Our method took between 55 seconds (FPLS) to 450 seconds (ALS) per densification. If faster computation time is required, it is possible to consider a smaller grid and a smaller resolution for the images at the price of a reduction in accuracy. Using  $9 \times 9$  grids and  $384 \times 216$  images leads to execution times between 30 seconds (FPLS) and 185 seconds (ALS). We observe substantial improvement between our results and reconstructions generated directly with Photoscan in terms of both geometric and photometric error for most models in the precise calibration case (improvement of approximately 0.4 mm for the geometric error and 0.1 in the DSSIM score for the best models). We also observe a small improvement between the reconstruction obtained without using shading (WS) and the others. We confirmed what was observed in the previous part even if differences are less significant: calibration of the light position slightly improves the results and SLS is still among the best models to use. Indeed, it produces very similar results to ALS while being much less complex. It also slightly improves the results obtained with PLS while not being much more complex. Both PLS and SLS behave properly even when only few images are available for calibration. On the contrary PLS is not robust and tends to generalise poorly even when more images are available.

## 5 Conclusion

We have discussed the need of photometric modelling in laparoscopic surgery. We have studied various light models and shown that the Spot Light Model, despite its simplicity, offers the best compromise between complexity and accuracy. This work is the first to systematically compare different light models, showing that there is an inherent trade-off between model complexity and benefit. Furthermore, as an example of photometry in a real usage, we have presented a novel dense shading stereo algorithm. We have shown two main results. First, higher complexity in the light model does not necessarily leads to better results, as some complex models tend to generalise poorly. Second, extremely accurate dense 3D reconstruction can be achieved by incorporating photometry, whose accuracy exceeds state-of-the-art dense multiview stereo. In future work we aim at extending the densification algorithm to merge multiple depthmaps, and to explore the use of photometry with deformable registration in laparoscopic AR pipeline.

## 6 Compliance with Ethical Standards

The authors declare that they have no conflict of interest. This chapter does not contain any studies with animals performed by any of the authors.

## References

1. Agarwal, S., Mierle, K.: Ceres solver. <http://ceres-solver.org>
2. Aggarwal, M., Hua, H., Ahuja, N.: On cosine-fourth and vignetting effects in real lenses. In: Proceedings Eighth IEEE International Conference on Computer Vision. ICCV 2001, vol. 1, pp. 472–479. IEEE (2001)
3. Bernhardt, S., Nicolau, S.A., Bartoli, A., Agnus, V., Soler, L., Doignon, C.: Using shading to register an intraoperative ct scan to a laparoscopic image. In: CARE, pp. 59–68. Springer (2015)
4. Collins, T., Bartoli, A.: 3d reconstruction in laparoscopy with close-range photometric stereo. In: MICCAI, pp. 634–642. Springer (2012)
5. Collins, T., Bartoli, A.: Towards live monocular 3d laparoscopy using shading and specular information. In: IPCAI (2012)
6. Collins, T., Bartoli, A., Bourdel, N., Canis, M.: Robust, real-time, dense and deformable 3d organ tracking in laparoscopic videos. In: MICCAI (2016)
7. Forster, C.Q., Tozzi, C.L.: Towards 3d reconstruction of endoscope images using shape from shading. In: Proceedings 13th Brazilian Symposium on Computer Graphics and Image Processing (Cat. No. PR00878), pp. 90–96. IEEE (2000)
8. Gallardo, M., Collins, T., Bartoli, A.: Dense non-rigid structure-from-motion and shading with unknown albedos. In: ICCV (2017)
9. Garrido-Jurado, S., Muñoz-Salinas, R., Madrid-Cuevas, F.J., Marín-Jiménez, M.J.: Automatic generation and detection of highly reliable fiducial markers under occlusion. *Pattern Recognition* **47**(6), 2280–2292 (2014)
10. Koo, B., Özgür, E., Le Roy, B., Buc, E., Bartoli, A.: Deformable registration of a preoperative 3d liver volume to a laparoscopy image using contour and shading cues. In: MICCAI (2017)
11. Land, E.H., McCann, J.J.: Lightness and retinex theory. *Josa* **61**(1), 1–11 (1971)
12. Langguth, F., Sunkavalli, K., Hadap, S., Goesele, M.: Shading-aware multi-view stereo. In: ECCV (2016)
13. Liu-Yin, Q., Yu, R., Agapito, L., Fitzgibbon, A., Russell, C.: Better together: Joint reasoning for non-rigid 3d reconstruction with specularities and shading. arXiv preprint arXiv:1708.01654 (2017)
14. Mahmoud, N., Cirauqui, I., Hostettler, A., Doignon, C., Soler, L., Marescaux, J., Montiel, J.: Orbslam-based endoscope tracking and 3d reconstruction. In: International workshop on computer-assisted and robotic endoscopy, pp. 72–83. Springer (2016)
15. Malis, E., Vargas, M.: Deeper understanding of the homography decomposition for vision-based control (2007)
16. Malti, A., Bartoli, A.: Combining conformal deformation and cook–torrance shading for 3-d reconstruction in laparoscopy. *IEEE Transactions on Biomedical Engineering* **61**(6), 1684–1692 (2014)
17. Mariyanayagam, D., Gurdjos, P., Chambon, S., Brunet, F., Charvillat, V.: Pose estimation of a single circle using default intrinsic calibration. In: ACCV (2018)
18. Okatani, T., Deguchi, K.: Shape reconstruction from an endoscope image by shape from shading technique for a point light source at the projection center. *Computer vision and image understanding* **66**(2), 119–131 (1997)
19. Parot, V., Lim, D., González, G., Traverso, G., Nishioka, N.S., Vakoc, B.J., Durr, N.J.: Photometric stereo endoscopy. *Journal of biomedical optics* **18**(7), 076017 (2013)
20. Stoyanov, D., Darzi, A., Yang, G.Z.: Dense 3d depth recovery for soft tissue deformation during robotically assisted laparoscopic surgery. In: International Conference on Medical Image Computing and Computer-Assisted Intervention, pp. 41–48. Springer (2004)
21. Wang, Z., Bovik, A.C., Sheikh, H.R., Simoncelli, E.P.: Image quality assessment: from error visibility to structural similarity. *IEEE transactions on image processing* **13**(4), 600–612 (2004)